Bull Mar Sci. 94(3):863–886. 2018
https://doi.org/10.5343/bms.2017.1134

research paper

Recognizing incipient epizootic shell disease lesions in the carapace of the American lobster, *Homarus americanus*

Joseph G Kunkel [1, 2 *]
Melissa Rosa [2]
Brian Tarbox [3]
Sabine Hild [4]
Michael J Jercinovic [5]
Ali N Bahadur [6]

[1] *Biology, University of Massachusetts Amherst, Amherst, Massachusetts 01003.*

[2] *Marine Sciences, University of New England, Biddeford, Maine 04005.*

[3] *Marine Sciences, Southern Maine Community College, South Portland, Maine 04106.*

[4] *Polymer Science Institute, Johannes Kepler University, Linz, Austria A-4040.*

[5] *Geosciences, University of Massachusetts Amherst, Amherst, Massachusetts 01003.*

[6] *Bruker BioSpin Corp., Billerica, Massachusetts 01821.*

**Corresponding author email: <joe@bio.umass.edu>, telephone (413) 335-6017.*

ABSTRACT.—Causal factors leading to epizootic shell disease (ESD) lesions in American lobster, *Homarus americanus* H. Milne-Edwards, 1837, are not well understood. We explore the structural and physiological bases for development of ESD from preclinical stages invisible to unaided eye to early visible stages. We present a lobster shell model, which develops structural functional vulnerability and suggests plausible routes to ESD. Medallions of carapace cuticle were obtained from carapace fixed with protocols to minimize movement of mineral and macromolecular components. Rapid processing of medallions was used to encourage large sample sizes compatible with environmental surveys. One- and two-dimensional analytic maps of polished sections of the cuticle, obtained with an electron microprobe, described the composite mineral and polymeric structures. Micro-Raman spectroscopy was used to identify bond properties of phosphates and carbonates, as well as signatures of organic structures. The frequency and properties of structures identified can be monitored through the lobster molting cycle using a high throughput application of micro-computed tomography (μCT). We observed density differences in the calcite layer, exocuticle, and endocuticle, and the frequency and structure of $CaCO_3$ structures in the endocuticle and membranous layer of carapace cuticle during chosen stages of the molting cycle. The correlative microscopy and μCT of shell structures provides improved understanding of the lobster cuticle structure. Detailed structural differences quantified through development and under different environmental conditions can provide insight into causes and vulnerabilities associated with ESD.

11th International Conference and Workshop on Lobster Biology & Management · Portland, Maine 4–9 June, 2017

Guest Editors:
Kari Lavalli, Richard Wahle
Guest Section Editor:
Donald Behringer

Date Submitted: 28 August, 2017.
Date Accepted: 12 March, 2018.
Available Online: 23 April, 2018.

American lobster, *Homarus americanus* H. Milne-Edwards, 1837, populations experienced increased and variable incidence of epizootic shell disease (ESD) (Smolowitz et al. 2005, Glenn and Pugh 2006) starting in 1978 (Castro et al. 2006,

© 2018 Rosenstiel School of Marine & Atmospheric Science of the University of Miami

2012). The basis of observed localized and variable ESD rates is not clear. Several causal factors have been suggested (Shields et al. 2012), including residual pollution from the 1996 North Cape oil spill (NOAA 2009), an association with industrial compounds, such as alkylphenols (Laufer et al. 2012), and rising mean temperatures south of Cape Cod (Tlusty et al. 2007). Irrespective of remediation efforts and causal factors, the lobster population south of Cape Cod has effectively collapsed leaving behind a remnant of the earlier fishery (Mandel 2016).

However, recent record harvests of American lobster have been recorded in both American and Canadian waters correlated with rising temperatures in the Gulf of Maine (University of Maine 2017) and lowered populations of top predators (Steneck and Wahle 2013). The phenomenon of global warming is being imposed on arrays of populations of species of Northern Hemisphere organisms that have responded with shifts northward (Perry et al. 2005). However, for the American lobster, moving northward was correlated with and included the population collapse south of Cape Cod, which was correlated with, and some think caused by ESD (Castro et al. 2012). The ESD-based decline of lobster populations south of Cape Cod is argued, mainly logically, on the observation that females carrying eggs delay their molting cycle giving shell disease lesions longer times to compromise the female carapace shell, and in addition, egged lobsters with ESD are observed to fail to survive molting at higher frequency than non-ESD egged females (Castro et al. 2012). While ESD frequency has increased markedly in the Gulf of Maine Lobster Management Zones A to G (map provided in Maine DMR 2017a), from historically low levels of one per thousand, the observation now is that the Gulf of Maine population remains relatively healthy with an ESD incidence below 1% overall (Maine DMR 2017a). However, in the southernmost Lobster Management Zones E, F and G, the level of ESD has risen to 2%–2.5% as reported 2012–2016 (Maine DMR 2017b). There are also independent reports of hot spots of ESD found in particular Gulf of Maine locations, where up to 1 in 5 lobsters are found to have ESD at its peak development seen in late fall and early spring, similar to the phenomenon of localized higher frequency observed in Buzzards Bay, MA (Stevens 2009). There is some urgency for practical, as well as theoretical, reasons in being able to detect shell disease at its earliest stages and to predict areas of imminent higher frequency. Until the earliest signs of shell disease can be discerned, the precise causes will be hard to identify.

The main objective of the present study was to develop a rapid high-throughput approach to evaluating lobster carapace architecture. We focus on structural and functional aspects of the shell to understand their potential for predicting the onset of ESD in Gulf of Maine populations. The dorsal carapace, the typical anatomical location where ESD is first seen, was chosen as the principle structure to be studied. An initial objective is recognizing the earliest stages of ESD but, more important, being able to recognize lobster vulnerability that will predict that ESD will develop. Our model population is in an area just outside the major islands of Casco Bay, Maine, which in our experience has in the past several years been a hotspot of ESD. In any location, harvesting a population sometime prior to peak ESD development could yield a substantially healthier crop that would be less marketable later in the season. Strategies for bringing product to market earlier or avoiding impoundment, during which shell disease might develop, could lessen the economic impact of ESD in particular seasons if the potential incidence could be predicted. We establish here the chemical and physical basis for understanding the structure of the lobster carapace

cuticle and, based on that structure, demonstrate a rapid approach to high throughput data collection and analysis for prediction of a population's future vulnerability to ESD.

Methods

Animals.—American lobster nonshell-diseased individuals were regularly collected from an area with low prevalence of ESD, inner Casco Bay (Maine DMR 2017a) in region F (43°43′N, 70°9.5′W). Though these inner Casco Bay animals typically did not display ESD, we were reluctant to identify them as totally ESD free given the reports of approximate 2.5% ESD prevalence in region F (Maine DMR 2017b). ESD-infected American lobster individuals were regularly obtained from traps at locations outside the major islands of Casco Bay, which from past experience we describe as having a high incidence of ESD. Each year, trap locations changed somewhat, but a typical year trap placement in 2013 is provided in map form as Online Figure S1, in which trap locations TB01–TB06 are considered "inner Casco Bay" and TB09–TB19 are considered "outer Casco Bay." In seasons 2014–2016, no ESD lobsters were found by us in inner Casco Bay from 40 traps hauled once per 4-d soak throughout the summer and into the fall. In outer Casco Bay traps, we could regularly find 20% of the animals with ESD. This allowed us to find animals with well-established ESD on the dorsal midline of the carapace that had more lateral cuticle free of ESD or with small ESD lesions. Subclinical lesions were sought in lobsters which exhibited well defined small lesions outside an area of more extensive existing lesions. This was based on prior experience of housing early-recognized clinical ESD animals and observing that new lesions developed in areas outside the current lesions that would have been described as subclinical or ESD-free. Outer Casco Bay trapped animals provided us with clinically identifiable ESD lobsters, such as the specimens seen in Figure 1, as well as ESD lesion–free animals that we describe as members of a vulnerable population. Lobsters were maintained in the UNE Marine Science Center life table with running fresh sea water averaging approximately 15 °C during the late spring and processed for sampling within days of collection unless they were maintained in the life table for later sampling. Maintained animals were fed twice weekly with Atlantic herring, *Clupea harengus* Linnaeus, 1758. Animals were euthanized at the end of the experiment by freezing. Samples of cuticle were obtained using a coring bit producing a 6 mm diameter medallion of cuticle (Kunkel et al. 2015, 2016). The four medallions from two ESD animals described here (Table 1) were compared to medallions from a historically ESD-free population (Kunkel et al. 2016) from outer Georges Bank, which were sampled at sea using the plunge freeze apparatus described below. Staging of the lobster molting cycle is taken from (Waddy et al. 1995).

Tissue Preparation.—Medallions of cuticle were obtained using a drill press (Micro-Mark MicroLux® Benchtop Variable Speed Mini Drill Press) with a 7 mm diamond coring bit, which produced 6 mm medallions of cuticle. All medallions were prepared following Kunkel et al. (2005, 2016). Specifically, medallions were plunge-freeze fixed in a −40 °C acetone bath with BioBeads to scavenge any released water and gradually returned to room temperature over a 24-hr period with several changes of cold anhydrous acetone. In the absence of water, the acetone was allowed to evaporate leaving a dry medallion. Some medallions were affixed to 26 mm plastic

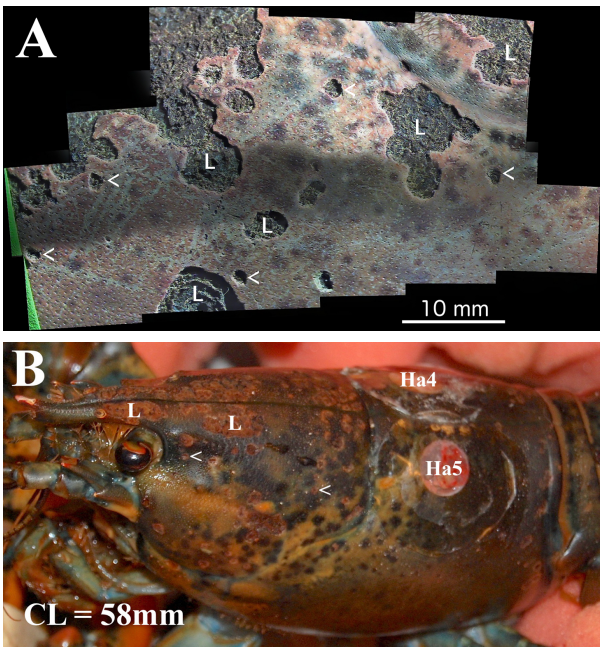

Figure 1. American lobster *Homarus americanus* shell diseased carapaces. (A) Montage of 22 light microscopy images of cuticle combined to demonstrate finding peripheral small-lesions (<) surrounding major lesions (L). Based on ImageJ measurement, these marked small-lesions are all above 1.5 mm in diameter. Their size can be judged relative to the original lobster in Online Figures S5A and S5B. (B) Live lobster carapace with measured CL of 58 mm has large merged lesions (L) around the medial dorsal suture, two smaller lesions marked (<) among many and two 6 mm medallion sampling locations, Ha4 and Ha5, patched on the medial lateral carapace. Medallion Ha4 was chosen to include the smallest of small lesions available, with diameter approximately 0.5 mm. Medallion Ha5 on the adjacent side had no superficially visible lesions when sampled.

Table 1. American lobster, *Homarus americanus,* used in the present study. Each specimen is a 6 mm medallion of cuticle collected using a coring drill, leaving a 7-mm hole in the carapace, and plunge-frozen in −40 °C acetone, and processed as described. Both epizootic shell disease (ESD) animals used came from outer Casco Bay.

Sample	Lobster	Description	Micro-computed tomography voxel dimension of sample
Ha4	C4 lobster with ESD	Right medial lateral carapace 6 mm medallion sample with a small 0.5 mm lesion with surrounding clear cuticle. The 7-mm hole in the carapace was patched as described (Fig. 1B).	1, 2.5, and 5 µm
Ha5	Same C4 lobster.	Left medial lateral carapace medallion sample one week later than Ha4 had clear cuticle with no apparent lesion. The 7-mm hole was patched as described (Fig. 1B).	1 and 5 µm
Ha6	Same C4 lobster	Right crusher claw face was sampled one week after the Ha5 Sample. The 7-mm hole was patched and the lobster maintained in a life table until it molted 2 mo later.	1 and 2.5 µm
Ha7	An ESD lobster was maintained in a life table until it molted. It was sampled 7 d after molting.	Right medial lateral carapace medallion was sampled from the postmolt completely ESD-free lobster cuticle.	1 and 2.5 µm

blanks, ground with carborundum paper to desired observation level, and polished with diamond polish (transitioning from 6 to 0.25 μm) to reveal planar views of cuticle structures as a polished face.

Data Collection.—Selected areas of diamond polished surfaces of lobster cuticle (Kunkel et al. 2012) and standards were submitted to both electron microprobe (EMP) (Cameca SX-50, and SX-100-Ultrachron, UMass Geosciences Microprobe Facility) and micro-Raman spectrometry (Horibe Jobin Yvon Aramis, JKU Linz AT, Polymer Science Institute). A limited number of area integral spectra were collected with the Thermo-Fisher Scientific DXR Raman Microscope.

Seven medallions of lobster cuticle were submitted to the Skyscan1272 (Bruker, MicroCT, Kontich, Belgium) for voxel data collection, three ESD-free medallions described in Kunkel et al. (2016) (Online Table S1; Kunkel et al. 2016), and an additional four ESD-associated medallions (Table 1). The collection of μCT voxel data at 8 or 16 bit density resolution from the 6 mm medallions required substantial memory as indicated by the tabulated file sizes and computation power. The analytic software AnalyzePro (AnalyzeDirect, Inc., Overland Park, KS, 66085), ImageJ (https://imagej.nih.gov/ij/), and R software (https://www.r-project.org/) required substantial memory and computation power and depending on protocols may access multiple cores when available. A MacBook Pro with 4 cores and 16 Gb of memory was used to do postdata-collection analytic computations. In many cases, data sets needed to be divided into regions of interest (ROI) to facilitate the analysis. When rotation of the data was necessary, DataViewer software (freely available from hardware manufacturers, e.g., Bruker) was used to subset, rotate, and save data to a new stack of 8 or 16 bit voxel slices in a new orientation. When rotation was not necessary, ImageJ was used to load desired voxel slices and crop them to a desired ROI, and saved as a stack with the same resolution or reduced resolution using ImageJ library functions.

Matrices of multivariate chemical composition data were collected from the Cameca-100 Ultrachron Electron Microprobe as raster arrays at 0.3 μm spacing (Kunkel and Jercinovic 2013) and by raster collection of 2800 element μm^{-1} spectra by the Aramis Raman spectrometer at typical 2 μm array spacing from 0.25 μm diamond polished sample surfaces. The multivariate data were processed by matrix algebra in R, which allowed using libraries that access multiple cores of the computer for operations that could use parallel processing. Principle component analysis was employed via singular value decomposition (svd) (Golub and Reinsch 1970) using the R function svd. Cluster analysis was performed on multivariate data using the k-means cluster function kmeans. PhotoStitcher (Maxim Gapchenko, iTunes) software was used to create montages of overlapping macro images of shell surface taken with a Zoomscope (Applicable Electronics, Cape Cod, MA) on a vibration suppression table with digital camera (IDS Imaging Development) using a translation stage (MicroMark, The MicroLux® X-Y Table) to position and move the specimen.

Data Collection Strategy.—Micro-computed tomography (μCT) reports 3-dimensional arrays of voxel density (Holstens and Laperre 2015) for lobster cuticle. The voxel slices from discrete volumes of cuticle can be analyzed slice by slice or as integrated volumes via analytic software. The large amount of voxel density data reported previously (Online Table S1; Kunkel et al. 2016) and new data reported here in Table 1, can provide insights into the coordinated structure beyond the limits of slices. Of particular interest to the present study was vulnerable carapace surface

structures: the epicuticular calcite layer and its intersection with the carbonate apatite organule canals, and interruption of either could produce vulnerable targets for microorganisms. Additional interest is focused on underlying structures, such as the trabecular-exocuticle, which supports the integrity of the surface calcite and canal structures (Kunkel et al. 2016).

A potentially high-throughput μCT protocol for lobsters was designed to study the carapace cuticle using the training set of seven lobster sample medallions, three from Kunkel et al. (2016; Online Table S1) and the four ESD associated medallions added here (Table 1). The samples were chosen to provide contrasts of potential targets for advanced understanding of the role of cuticle structure in vulnerability to ESD and to allow early detection. In the present study, the seven training set medallions of lobster cuticle were scanned at various resolutions (0.5, 1, 2.5, and 5 μm). Of the ESD-associated μCT data sets, six were from lobster carapaces from two of the four potential sample categories presented in Table 1. Three medallions were collected from a single late-intermolt (C4) lobster with advancing ESD (Fig. 1B), one from the dorsum of the large chela (with an ESD lesion), and two from the carapace, one carapace medallion with a visible small lesion and another from adjacent carapace subclinically lesion-free. A second ESD lobster was maintained until it molted, becoming subclinically free of ESD, and was sampled 1 wk post molting. Three medallions from clinically-lesion-free lobsters at intermolt (C4) were obtained from control non-diseased lobster populations, i.e., the outer edge of Georges Bank (Kunkel et al. 2016).

One provisional strategy to recognize incipient ESD lesions is to extrapolate back to the earliest ESD lesions recognizable by the naked eye and characterize their development, and additionally look in the sampled neighborhood for subclinical lesions using the high resolution and volume sampling of μCT. To do that, we typically took the carapace (e.g., supplementary macro image in Online Fig. S2A) of a clinically ESD–infected individual and looked on the periphery of its well-developed ESD lesions with light microscopy (shown in Fig. 1A) to see smaller lesions that, from past experience, will develop into larger ESD lesions. Using the high ESD–incidence population lobsters in outer Casco Bay, we selected an individual stage C4 lobster (Fig. 1B) in which an approximate 500-μm lesion was identified and included in a carapace medallion, Ha4, and another medallion free of LM visible lesions, Ha5, was collected from the contralateral position of the same animal (Fig. 1B). We also selected another lobster that had substantial ESD, and which was close to molting, to bring into the laboratory to record the day of molt, allowing us to sample the animal at a specific time postmolt, Ha7.

Results and Discussion

Chemical Analyses.—Chemical properties of lobster carapace cuticle architecture were obtained by applying two exemplar chemical analytic tools to polished cuticle surfaces. First, using a high resolution electron micro-probe, the carbonate apatite exocuticle trabeculae in the lobster carapace exocuticle was observed by its pattern of elemental proportional composition in polished tangential sections of an exocuticle layer. The phosphate (Fig. 2A) is seen in a trabeculum-like pattern on a more uniform pattern of Ca^{2+} (Fig. 2B). Some phosphate rich areas of Figure 2A have apparent dense cortices with medullas with lowered phosphate density. From

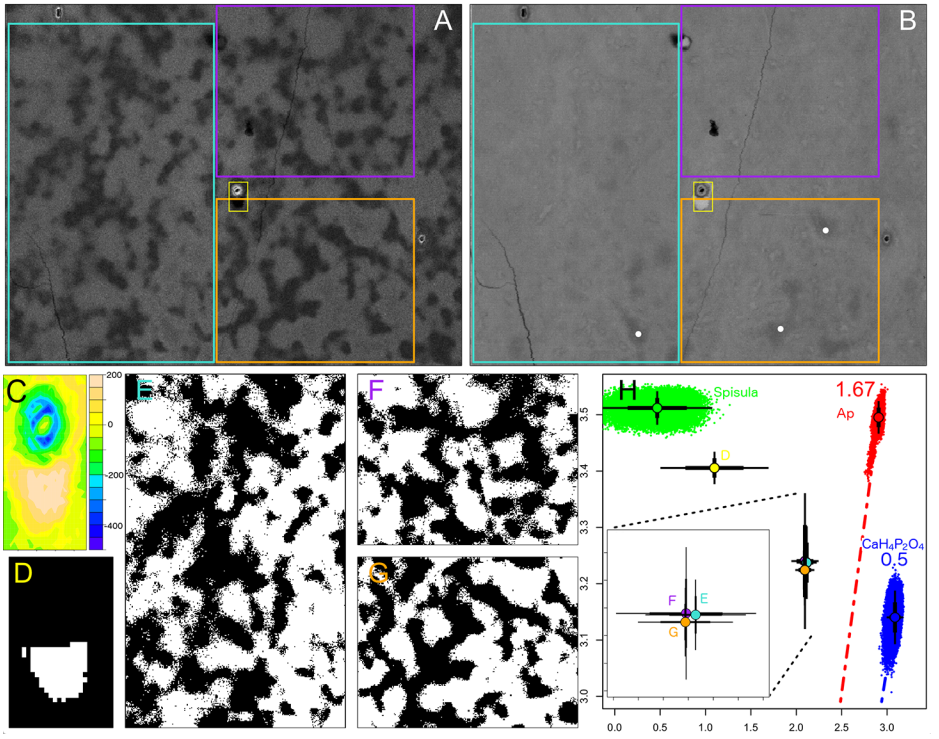

Figure 2. Selected area analyses of Ca, P, and Cl data for trabeculae separating and surrounding three primary organules seen in a tangental polished section of lobster cuticle through the inner exocuticle. (A) Phosphate image with four subareas identified by rectangular boxes. (B) Calcium image similarly divided. Low Ca cores are marked with a white dot. (C–G) Subareas of panels A and B analysis. (C) svd_{Ca} of the organule data enclosed by yellow rectangles in panels A and B. (D) A mask created by choosing pixels identified with $svd_{Ca} > 100$. (E–G) The masks identifying phosphate-rich pixels of three areas of panel A and B produced with $svd_{P} > 25$. (H) Log Ca vs log P with the same standard of fluoroapatite (red line with Ca/P of 5:3), clam shell (green with Ca/P of 1:0), and $Ca(H_2PO_4)_2$ (blue line with Ca:P = 0.5). The three sample areas of trabeculae have their means and 1 (broad bar) and 1.96 (thin bar) standard deviations corresponding to 64% and 95% confidence intervals of the data computed on a log normal basis.

geometrically identical sectors of Figure 2B (the calcium signal), one can recognize corresponding medullas with lowered calcium densities (marked with a white dot). This suggests organized trabeculae develop with cortices of high Ca and P, but lower Ca and P at their medulla, a developmental phenomenon that may conserve P and could be confirmed with high-throughput sampling and analysis based on measuring density variation with the more rapid μCT approach. This analysis was extended to examine other fine resolution tangentially cut structures, such as the dermal gland canals (Fig. 3), where an organule canal wall is seen to use two distinct ratios of Ca:P, 2.67 and 2 (Fig. 3E, F) in discrete layers, and a third distinct ratio, 3.5, in a secondary-canal wall (Fig. 3C, D).

The patterns of elements used in constructing the carapace can be teased apart using k-means clustering of pixel-wise composition matrices producing a map of clustered pixel types and displayed in raster or bar-chart format (Fig. 4). K-means clustering uses a Monte Carlo approach that requires several iterations of clustering to establish a consistent result. However, its output provides additional insights into

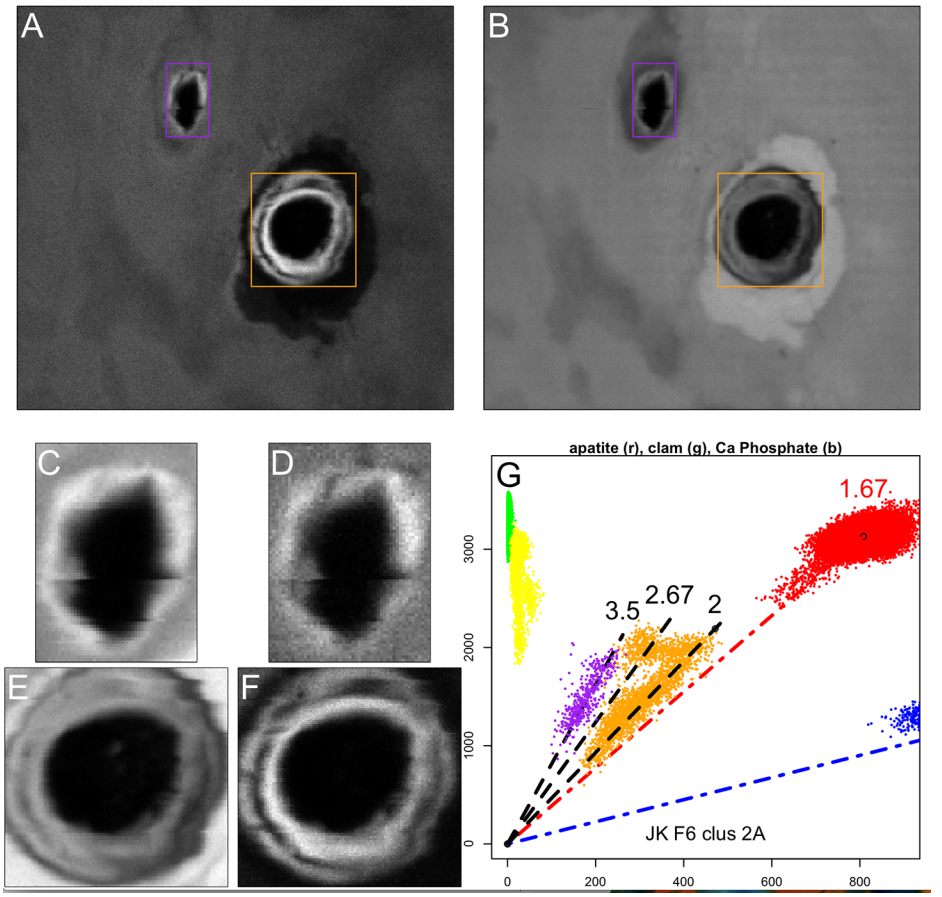

Figure 3. Selected area analyses of Ca and P for a secondary organule seen in a tangental polished section of lobster cuticle through the inner exocuticle. (A) Phosphate image. (B) Calcium image. (C–F) Selected areas of panels A and B analyzed by singular value decomposition which allow apatite and calcite pixels to be identified. (G) A scatter-plot of apatite pixel Ca and P vs each other with a standard of fluoroapatite (red with Ca/P 5:3 =1.67), clam shell (green with Ca/P of 1:0), and Ca(H2PO4)2 (blue with Ca:P slope 0.5). The CAp of the large canal, panels E and F, displays Ca:P dual ratios of 2 and 2.67 (orange), while the smaller canal in panels C and D displays a single ratio of 3.5 (purple). The Ca rich (yellow) enclosing sheath of the canal seen in panels B and E is likely an organule socket cell product.

the carapace structure, e.g., chloride distribution in the endocuticle is seen to oscillate significantly in synchrony with the Bouligand layers of cuticle (Fig. 4C), while the calcium, phosphate, and Ca:P ratios are not significantly different (Fig. 4B, D, E). It is likely that the chloride content is a basis for endocuticle Bouligand layers being clustered differently, which is repeated in all iterations (not shown) of the k-means clustering algorithm. Three observed k-means clusters regularly spanned the phosphate rich trabeculae, seen as the three bars labeled *Canal, Nipp,* and *Lam_2* (Fig. 4), because they characterize: (1) the majority of the length of the dermal gland canal wall and the cortex of the trabeculae (yellow); (2) the next most phosphate rich structure, the nipple structures (violet), which characterize and surround the exit of the dermal gland canals on the basal side of the cuticle; (3) the lowest phosphate rich structures (brown) which form a continuum with the endocuticle clusters and share

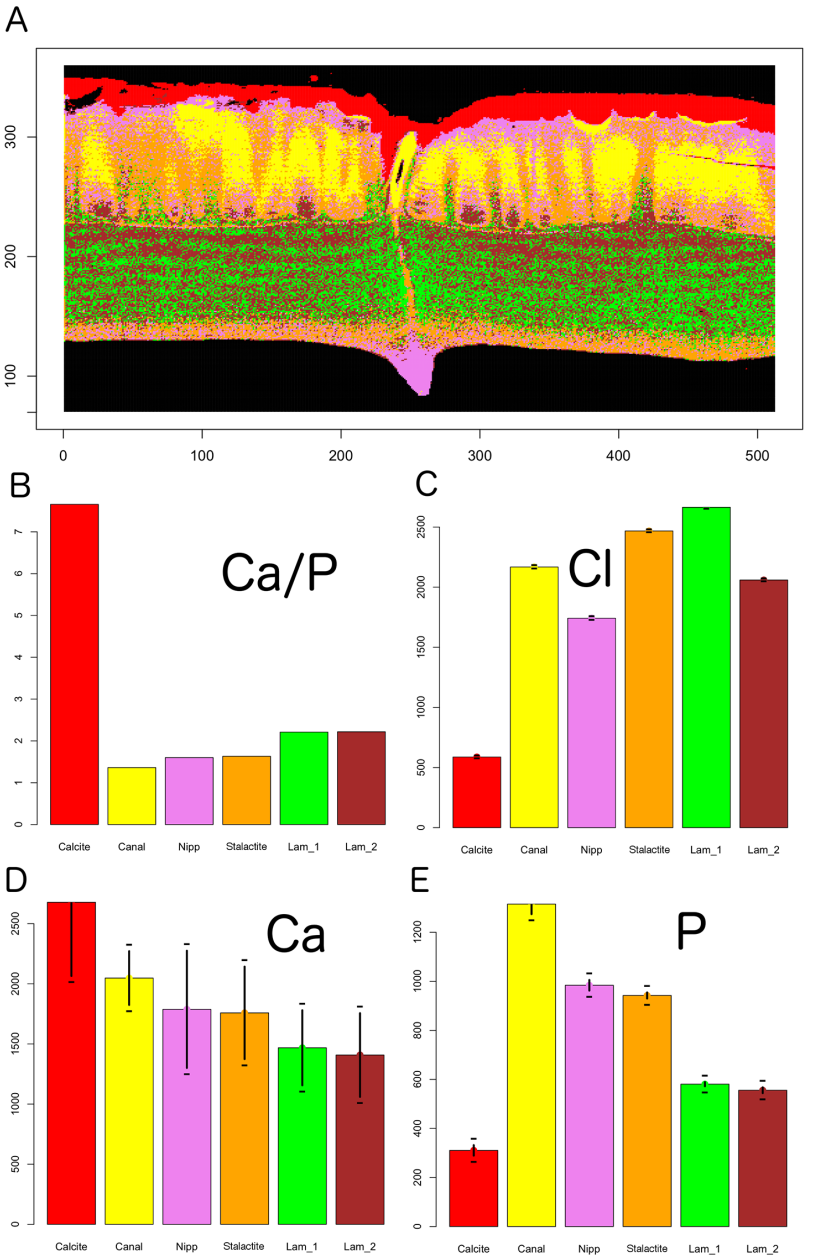

Figure 4. K-means cluster analysis of carapace cuticle electron micro probe (EMP), alternate analysis of Kunkel et al. (2013, fig. 3) data. (A) One of 25 independent iterations of a 10-mean clustering of EMP compositional data of American lobster C3 carapace polished cuticle section. Six clusters (four ignored clusters were external densities and coded black) span the cuticle structures which are given colors and names typical of their location. The calcite cluster is red and has the highest Ca:P ratio being highest in Ca and lowest in P. The canal cluster is yellow but shares its cluster with trabeculae. The nipple cluster is violet and also shares its cluster with trabeculae. The stalactite cluster is light brown. The Lam_1 cluster is green. The Lam_2 cluster is dark brown. Barcharts comparing the cluster properties are presented as panels B–E. (B) Ca/P ratios of the cluster pixels. (C) Chloride content of cluster pixels. (D) Calcium content of cluster pixels. (E) Phosphate content of cluster pixels.

with them an enrichment with chloride (Fig. 4A). The k-means clusters create cartoons of the trabecular cortices and medullas referred to in the previous paragraph. The yellow cortex around a lavender medulla surrounding the dark-brown inner medulla form patterns replicated through the exocuticle of Figure 4A, characterizing the trabecular structures. The light brown stalactite material extends from the calcite layer toward the endocuticle and typically merges with dark brown material of the endocuticle layers. Both light and dark brown cluster pixels are lower in chloride.

Given that this k-means cluster analysis only covers the three elements, Ca, P, and Cl, it is possible that distinctive properties of shell structures are established by other elements or chitin and layer-specific protein polymers that participate in the structures. For example, it is known that fluoride modifies the luminal surface of dermal gland canals of both *H. americanus* and *Homarus gammarus* (Linnaeus, 1758) (Kunkel et al. 2013), perhaps participating in a similar hardening of carbonate apatite as generally recognized for vertebrate teeth and bones. In addition, Mg participates in the calcite layer more so than in the $CaCO_3$ rich structures of the exocuticle, endocuticle, and membranous layer (Kunkel et al. 2012).

A major insight into the chemical differences between carapace cuticle structures can be obtained from a second analytical method, micro-Raman spectroscopy. The wavelength of the laser photon stimulus is re-emitted as characteristic Raman-shift photons, which characterize the molecular bond vibration emitting the photon. The bonding-signature Raman-shifts of carbonate, phosphate, and organic structures were evaluated in polished sections of carapace cuticle at an approximate 2 μm resolution using the Labram Aramis micro-Raman spectrometer with auto-focus and auto-cosmic-ray-filter. Figure 5 illustrates average spectra whose constituent spectra were identified from the raster of collected spectra and were identified using svd analysis. The canal wall of a dermal gland (Fig. 5A), was identified using svd (Fig. 5B), and a mask created (Fig. 5C) picking the spectra to average. The canal wall spectral averages (Fig. 5D-c) showed spectral signals at ν1, ν2, ν4 of PO_4^{3-} and ν1, ν2, of CO_3^{2-} consistent with carbonate apatite (Online Table S1).

Similarly, the canal lumen exhibited spectra with a dominant peak at wavenumber 1318 cm^{-1}, which when averaged (Fig. 5D-a), suggests the canal luminal secretion contains the CH bonding of protein chains. The rings surrounding the canal wall represent alternating phosphate rich and $CaCO_3$ rich bands, which when averaged, provide respectively the trabecular-like spectra (Fig. 5D-e), and $CaCO_3$ spectra (Fig. 5D-d). Reference bone and aragonite samples are analyzed to provide positive controls of standard Raman spectral shifts.

Signatures of chitin and protein polymer residues are more clearly seen in Online Figure S3, which has its wavelength axis extended to 3500 cm^{-1} and includes the broader ch-stretch regions surrounding 2883 (chitin), 2935 (CHO polymers), and 2965 (protein side-chains). In addition, Online Figure S3 demonstrates the Raman spectra of the carapace calcite layer, showing its lack of any substantial chitin spectral signal, which characterizes it as a cuticular pre-chitin-synthesis product, marking it as part of the epicuticle.

Other analytical techniques can be applied to 2-D polished surfaces of cuticle sections, such as micro-Fourier transform infrared spectroscopy to examine bonding (JG Kunkel unpubl data), polarized light microscopy to examine the calcite layer thickness and orientation (Kunkel et al. 2012), and atomic force microscopy to examine layer structure textures (Kunkel 2013). These techniques are useful to further

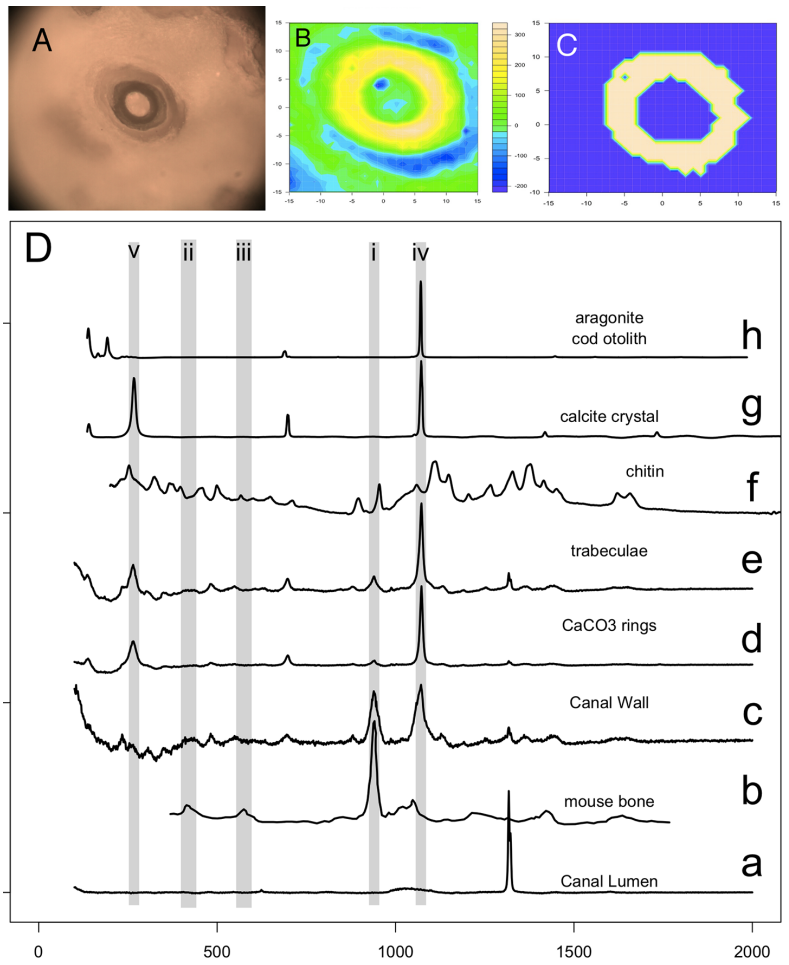

Figure 5. Raman spectra of selected areas of lobster cuticle seen in tangental polished section, neonatal mouse bone, purified crab chitin, calcite crystal and cod otolith aragonite standard. (A) Light microscope image of canal. (B) svd 3 contrasting the canal wall with other surrounding structures. (C) Mask identifying locations of spectra with svd > 200. (D) Line a is lobster dermal gland canal lumen average of 38 spectra; b is mouse bone data from Kavukcuoglu et al. (2008); c is canal wall average of 172 spectra; d is $CaCO_3$ ring average of 84 spectra. Line e is cuticle trabeculae; f is chitin standard; g is calcite crystal; h is cod otolith aragonite standard average of 25 spectra. Gray highlighted zones: i = v1 PO_4, ii = v2 PO_4, iii = v3 PO_4, iv = v1 CO_3, v = v2 CO_3

understand the properties of cuticle layers, but are similar to all other 2-D surface approaches in being too time consuming in preparation and measurement to allow high throughput data collection. However, these 2-D chemical-analytic approaches allow us to pursue identified and characterized structures using the more rapid X-ray scanning of cuticle voxel density available via µCT.

Exploring Shell 3-D Density using µCT.—Lobster shell medallion samples for µCT analysis can be produced, scanned, and the resultant data analyzed to produce 3-D voxel density data files in a high-throughput mode (18 samples per day) using plunge-freeze fixation and an automatic sample loader of the Skyscan 1272 µCT. The

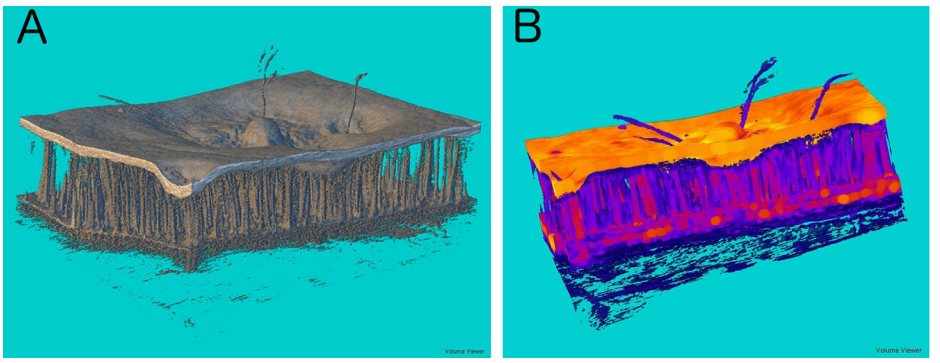

Figure 6. Region of interest (ROI) of medallion Ha7 with an actively secreting organule with secretion streams captured as X-ray densities. (A) Oblique view of the ROI interpreted with ImageJ Volume Viewer plugin. (B) Oblique view of the ROI interpreted with the ImageJ Bone Thickness plugin with lighter toned structures are thicker.

interpretation of the gigabytes of data from each sample could limit the speed with which structures within the voxel density data can be identified and analyzed. We used an initial exploratory mode to identify software and analytic approaches that could be useful in understanding the structures involved, as well as approaching high-throughput speeds for studying natural populations of lobsters.

The surface of the carapace seen on a 1-wk postmolt medallion shows regularly spaced organules. Online Figure S4 shows the entire early postmolt Ha7 medallion scanned at 2.5 μm with μCT. Freeze fixation was able to fix an apparently active stream of secretion coming from openings of the dermal glands of primary and tertiary organules. These freeze-fixed streams of material likely correspond to additions to the "cement" layer described by Wigglesworth (1948) and Locke (1961) as postmolt dermal gland additions to the epicuticle. We suggest that a secretion, dense enough to be profiled by the X-ray beam, is fixed in the process of being distributed onto the epicuticle surrounding each dermal gland. Figure 6A illustrates a ROI of the Online Figure S4 medallion processed with the ImageJ Volume Viewer plugin showing a tertiary organule with four streams of material emanating from dermal gland canals. In Figure 6B, the voxels are analyzed by the "Thickness" routine of the BoneJ plugin of ImageJ, which fits spheres of largest possible radius into voxel volumes defined using a 3-D binary segmentation of the X-ray densities. The diameter of a circle fit into a 3-D segmented space is presented as a graded-color, small-(dark/purple) to large-(light/yellow). This automated segmentation technique, filling the segmented spaces with graded circles, is relatively time consuming in machine time when applied to an entire stack of voxel slices, but provides insight into the uniformity of structures and their thicknesses, and could be applied to a small selection of slices to save time. The Figure 6 demonstration of a thickness measure was carried out in ImageJ, including preprocessing by an initial density segmentation to a binary interpretation of the grayscale density after various levels of smoothing of the voxel data to fill interfering natural-low-densities in otherwise regular structures. This preprocessing adds a time-consuming step of required investigator attention. The thickness of the elements of the circle-filled 3-D binary structures can be characterized by statistics on the circle diameters or visually as in Figure 6B.

The binary segmentation and thickness analysis protocol, applied to the 7-d postmolt data, suggests that the calcite layer of the post molt carapace is initially

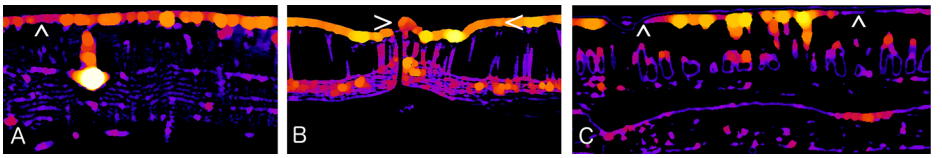

Figure 7. Micro-computed tomography (μCT) of three American lobster, *Homarus americanus,* carapace medallions with their voxel densities interpreted with the Bone Thickness Plugin of ImageJ. (A) Region of interest (ROI) of C4 lobster Ha4 from an epizootic shell disease (ESD) free zone. Caret (^) shows a region of relative thinning of the calcite layer. (B) ROI of 7-d post molt medallion Ha7 from a lobster with ESD in prior stage. The bright continuous calcite layer (<) is thick even at the interface with the organule canal (>). (C) ROI of a no-lesion-medallion Ha5 from the ESD lesioned C4 lobster medallion. Lighter color illustrates thicker layer. The carets (^) show regional thinning (coded darker) of the calcite layer that could indicate vulnerabilities to ESD, which is nowhere seen on this medallion Ha5 with the exception of a ROI suggested to be a possible incipient lesion, and investigated in Figure 8A,B and seen in Online Figure S6 (and its linked video).

relatively uniform in thickness throughout the viewed surface despite it being from a prior ESD individual. The same thickness-evaluation protocol was applied to three medallions illustrated in Figure 7. One sample was from C4 lobster medallion Ha2 (Kunkel et al. 2016) that did not display any lesions anywhere on its carapace (Fig. 7A). A second medallion Ha7 (Fig. 7B) was from a lobster 7 d after a molt that had displayed substantial carapace lesions in the prior instar. A third medallion Ha5 (Fig. 7C) did not display lesions on its 6 mm diameter surface, but was from a C4 lobster that was displaying ESD carapace lesions elsewhere on the carapace. It is clear that the Ha5 medallion (Fig. 7C) from an active ESD lobster had thinned calcite regions in its apparently non-lesioned areas of the carapace. The apparently-healthy Ha2 lobster cuticle (Fig. 7A) shows relatively uniform thickness calcite layer and the recently molted medallion sample Ha7 (Fig. 7B), molted from a formerly ESD lobster, also showed a uniform thickness calcite layer. The serious degree of thinning seen in the Ha5 (Fig. 7C) medallion is emphasized by Online Figure S4 link to a movie displaying an entire stack of the thickness interpretation of the middle zone of the complete hemi-medallion at 2.5 μm resolution showing 1450 slices of the thinning phenomenon. While convincing, such comprehensive coverage is time consuming to calculate (at least 1 d of preprocessing to create a binary segmentation of the calcite layer for each entire medallion sample) and evaluate. A potentially automatic ImageJ protocol for preprocessing random voxel sections could logically be developed to speed this approach to a level that might allow high throughput.

Both the Volume Viewer plugin and Bone Thickness plugin of ImageJ provide their insight at a substantial time cost, partly due to many of the decisions needing to be made by a human operator and partly due to the immense number of calculations that need to be done if the operator chooses comprehensive analysis of all the data, which would be statistically over-scrupulous and impossible to use as a high-throughput protocol. Similarly, a commercial medical software, AnalyzePro, was used to segment the data into density defined surfaces that provide useful insights into the carapace architecture by creating stl files, which were used to display the surfaces selectively as digital images. For example, Figure 8 illustrates AnalyzePro-produced stl files of the calcite layer and of the trabeculae of two late intermolt, stage C4, carapace medallions of an ESD lobster, the Ha5 medallion (Fig. 8A, B) only superficially lesion free and shown in Online Figure S5, which links to a video, where a hint of a subclinical lesion is suspected as a segmented white patch visible during

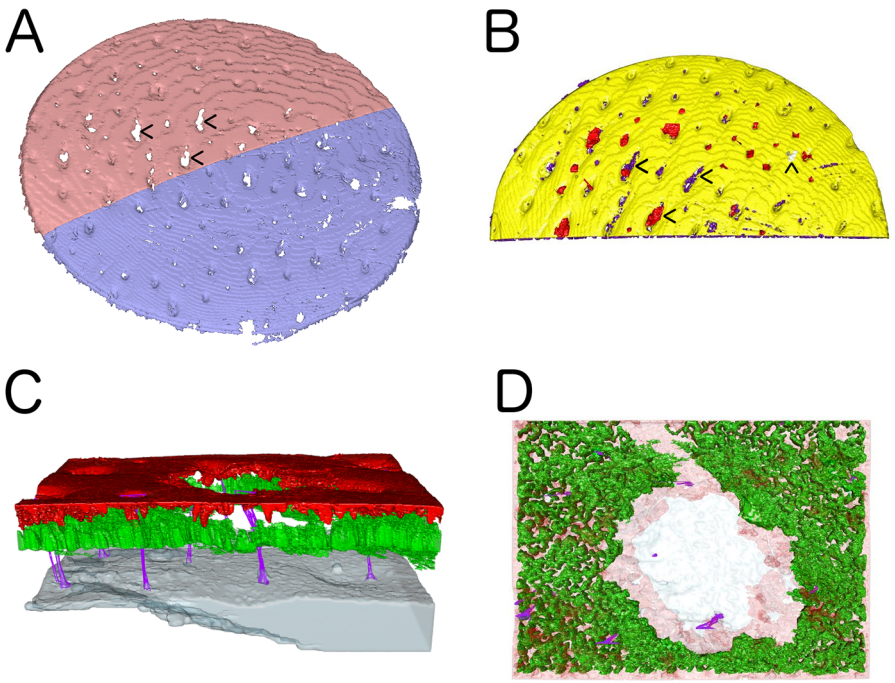

Figure 8. Structural surfaces of American lobster, *Homarus americanus,* carapace cuticle defined by stl files extracted from micro-computed tomography (μCT) of epizootic shell disease (ESD) infected lobster carapace medallions. (A, B) Imagery from 6 mm diameter medallion Ha5 that shows no apparent lesions. (C, D) Imagry from both a ROI from medallion Ha4 with a 500 μm diameter ESD lesion. (A) Image is 2.5 μm resolution μCT scan that needed to be divided into two hemi-medallion data sets, which were analyzed in AnalyzePro and re-assembled in Meshlab. Potential areas of vulnerability are indicated (<) based on the localized thinned (pink) stl file expression of the calcite layer. (B) stl files of the calcite and trabeculae are viewed obliquely using an R-library to read and plot stl defined surfaces. A caret (^) indicates a possible incipient ESD lesion color coded in white. Potential areas of vulnerability are indicated (<) based on the localized thinned (yellow) stl file expression of the calcite layer. These are the same vulnerabilities indicated in the panel A pink sector. (C) ROI of the ESD lesion as seen with stl file defined density structures of calcite layer (red), trabeculae (green), membranous layer (gray) with outlines of recognizable canal paths (purple). (D) Same as panel C viewed from above through an imposed transparency of the calcite layer.

rotation. The Ha4 medallion (Fig. 8C, D), exhibits the smallest superficially-visible lesion we have studied in detail so far. The stl surface plots were embellished with outlines of its dermal gland canal structures obtained with the ImageJ line tracing function, which allows tracing of an object through a stack of slices. One feature of the medallion ROI (Fig. 8C, D) and the videos of the rotating structures (provided in Online Figure S6) is the thinned calcite layer, as segmented in ImageJ at a chosen density of calcite, and seen to be very thin in several areas. One can see through fenestrations of the calcite-segmentation to what would be a next layer down, the exocuticle stalactite densities, which we did not visualize in Figure 8C and D. However, we do see the visualized trabeculae further below in the Online Figure S6, particularly when in motion in the Online Figure S6 linked video. Again, this segmentation approach producing stl files is expensive as a commercial software and in analysis time, taking on the order of two computation days for each medallion examined with Analyzer Pro on a fast computer (2.5 GHz, 8 cores) with large memory (16 Gb). It

also requires substantial interpretation time to view the motion videos and visually interpret the thinned fenestrated surface. While some economy of effort and time might be achieved when the segmentation of interest is reduced to routine, it is unlikely that this approach would provide successful high-throughput discrimination between healthy and ESD prone cuticle. However, it does direct one in this case to focus on developing a protocol to measure the thickness and density of the calcite layer in a random way to capture the generally pervasive calcite-layer-thinness that may be associated with vulnerability to ESD.

A rapid measure of calcite layer properties was applied using a standard protocol of ImageJ. Specimen density can be measured along a linear transect averaged with a chosen scan path pixel-width. This approach uses the ImageJ decision path, Analyze/Plot Profile, to record a linear path oriented perpendicular to the cuticle surface through all the layers and routinely including a reference crystal material (Fig. 9). This approach is relatively easy to implement on medallion voxel sections. It can be automated using a Java Macro defined as an ImageJ plugin. Such an approach would produce data transects (stored as csv files) of voxel density in a linear path through the cuticle, which could be viewed individually (e.g., Fig. 9A–C) or used to provide statistics on the average calcite layer thickness or density distribution (Fig. 9D) for each medallion. The ROIs need to be identified manually by an operator in the chosen scans (Fig. 9A,B), scanned with the ImageJ Analyze/Plot Profile function and the saved profile integrated with an R script function. Figure 9 data includes 318 ROI density averages covering standards, unknowns, and baseline. The resultant relative data were analyzed by analysis of dispersion and the multivariate test of additional information (Rao 1965) implemented in R. The log densities of the scanned included mineral standards (apatite, calcite, KH2PO4, and K phthalate) were used to create a standard curve from the parallel 8- and 16-bit data, which was used to estimate the apparent densities of the epicuticle calcite layer and endocuticle measure densities. The barchart of Figure 9D averages over the operational variables bit-depth and scan-width to provide estimated mineral densities for epicuticle and endocuticle for the four ESD medallions and three μCT densities (1, 2.5, and 5 μm). It shows, with the means and 95% CI, a largest estimate for epicuticle density when using the highest resolution voxels (1 μm) and a significant trend down with voxel size. This is logical since the epicuticle is a thin layer to begin with and the width of the scan process can blur the peak of density of the thin layer. The endocuticle shows less of that inverse relationship, which is also logical given it is a thick layer and the resolution should not matter. This is confirmed by a test of interaction between resolution and cuticle layer, which was very highly significant ($P < 0.001$). The covariates of data bit size (8 vs 16) and linear scan path widths (4, 8, 16, 32, 64, 128, and 256) chosen in ImageJ did not add any additional information ($P > 0.5$) in estimating the averages of either epicuticle or endocuticle. In a separate series of scans (not shown), scan path width did provide a more stable mean based simply on increasing the number of voxels averaged, but did not significantly change the average densities measured. That means one can use the largest scan width that provides the best coverage of a voxel slice and shell layering without including surface features, such as pits and gland canals. Using this approach on random μCT voxel sections of each of 18 medallions, one could process all the medallion data scanned overnight potentially during the following day.

In this case (Fig. 9) of limited samples, the overall densities of the four medallion epicuticle-calcite-layers were only modestly different, which is reasonable given that

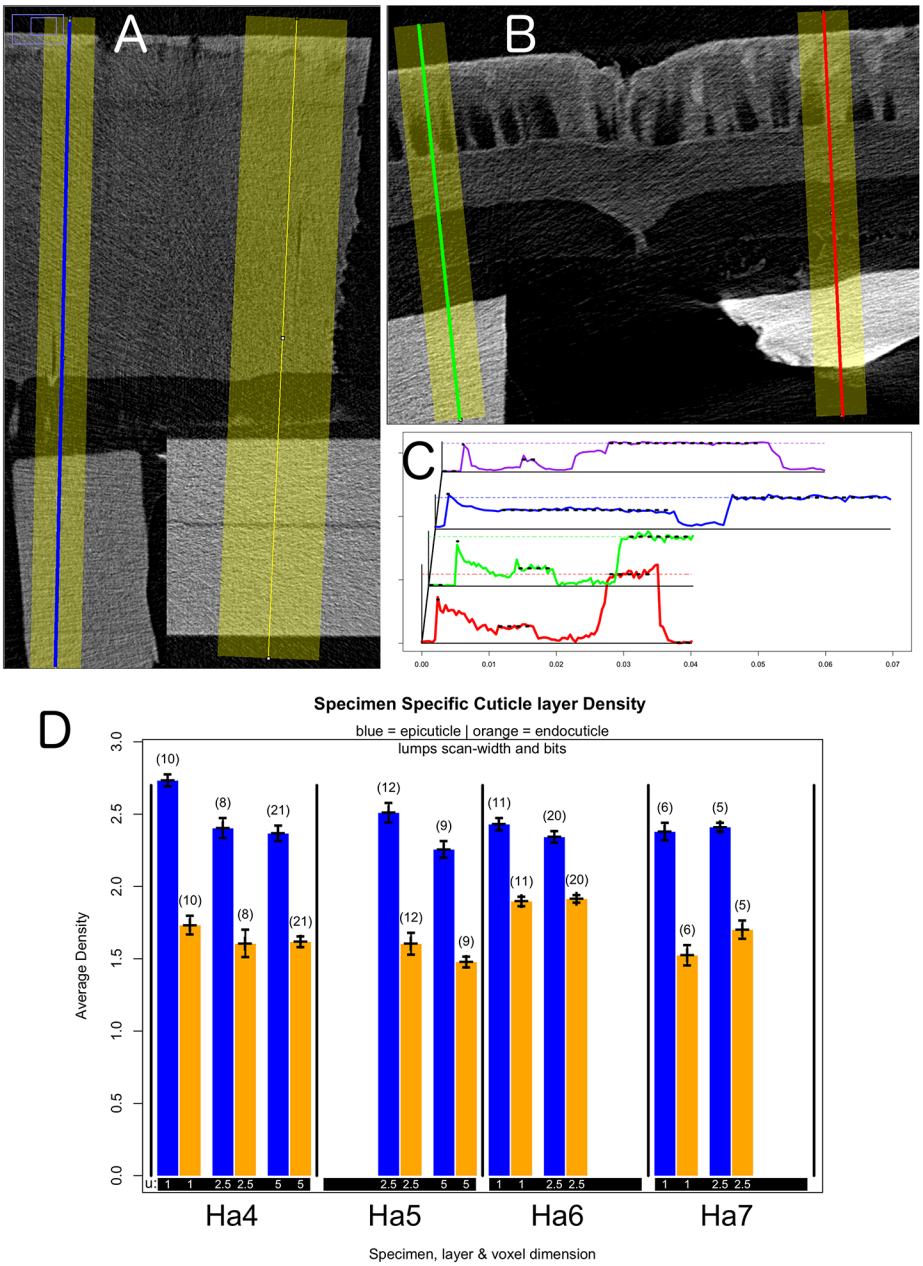

Figure 9. Analysis of X-ray density of cuticle layers obtained by ImageJ line scans. (A) Image and scan track of Ha6 voxel slice from a dorsal "crusher" chela with 128 µm and 256 µm wide line scan-tracks. (B) Image and scan track of Ha4 voxel slice from dorsal lateral carapace with two 128 µm wide scan-tracks. (C) Running averages of the voxel density along transects the R, G, and B lines (illustrated with coordinated colors in panels A and B) showing sectors of averages for epicuticle, endocuticle, standards (apatite, calcite, KH_2PO_4 and zero-baseline density), which were averaged to produce a single datum for analysis of variance. (D) A barchart of epicuticle density (blue) and endocuticle density (orange) focusing on the effect of micro-computed tomography (µCT) resolution on the measurement of epicuticle and endocuticle layer density. Means with 95% CI are plotted. Sample size is displayed parenthetically above the CI bar. The microCT resolution is listed for each specimen on the *x* axis.

medallions Ha4, Ha5, and Ha6 were from the same C4 stage lobster. The Ha7 medallion was from a recently molted lobster, but its calcite layer and endocuticle still had characteristic densities similar to the Ha4, Ha5, and Ha6 medallions. There was a significant interaction between specimen, layer, and density, which emerges in the barchart in Figure 9D as a visible carapace vs chela endocuticle density difference. The chela endocuticle is substantially denser, as well as being measurably thicker, which mark the chela as a potential site of both calcium and carbonate storage, some resorbed before molting, the remainder eaten soon after molting.

The appearance of lobster populations with carapaces exhibiting some measure of thinned calcite layer or reduced storage density of minerals in any of the shell layers of exo- or endocuticle could be predictive of vulnerability of that population to shell disease. This predictive approach would depend on validating the prediction using populations that are systematically followed and carapace medallions sampled, subjected to μCT, and properties of the cuticle correlated with the ensuing history of that population with respect to ESD. The present phase of the study demonstrated an ability to collect quantitative density data that can be analyzed using factorial design and allows significance testing to measure effects of environmental factors on cuticle properties.

Recognizing Incipient ESD Lesions.—To identify a causative agent of ESD, we would need to extrapolate to an earliest lesion and identify its association with some causal factor. We have attempted to do that and were frustrated in how time-consuming the extrapolation would be when applied to candidate populations. Observations that led to that conclusion follow.

We constructed an ImageJ Volume Viewer interpretation of μCT data from an individual stage C4 lobster (Fig. 1B) carapace medallion Ha4 (displayed in Fig. 10A), which included an approximate 500 μm ESD lesion. Medallion Ha5 was extracted from a symmetrical position across the midline and was superficially free of lesions. Both medallions were examined for calcite layer density and thickness. In addition, medallion Ha6 was sampled from the large chela of the same animal, which also had a small ESD lesion. The density reconstructions of the surfaces are illustrated in Figure 10.

Figure 10A illustrates the smallest clearly recognizable ESD lesion we have visualized with μCT so far. It is typical of carapace ESD lesions in showing a cylindrical penetration through the epicuticle and exocuticle. The same ImageJ visualization protocol was applied to a larger lesion on the chela medallion (Fig. 10B). The conical chela-lesion has a diameter at the chela cuticle base surface of 250 μm and widens to 1500 μm at the cuticle surface. This chela lesion illustrated (Fig. 10B) is dominated by the conical endocuticle erosion at a late stage in the ESD development process. Further effort was made to search for lesions in the cuticle sampled from the carapace of this shell-diseased lobster that had surrounding cuticle with advanced ESD lesions. One somewhat questionable and much smaller potential lesion is seen as a departure from regular texture interpreted by Volume Viewer in Online Figure S5. That lesion is of possible further interest in that it potentially shows a decrease in mineral density ballooning internal to the outer surface that could signal some type of penetration through a narrow imperfection in an otherwise relatively tight calcite layer surface. Searching for such irregularities as candidates for the origin of an ESD lesion is fraught with many subjective decisions based on subtle visual interpretations, and we did not see this approach as plausible to follow in a quantitative way.

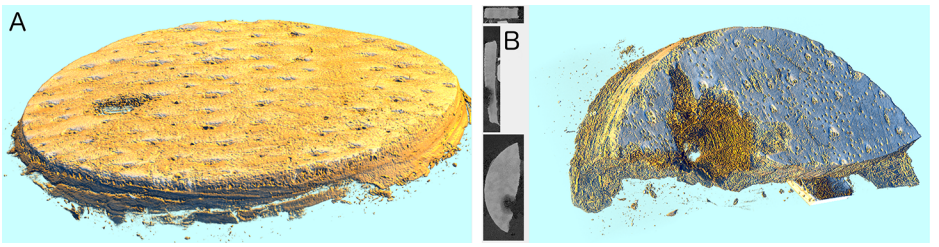

Figure 10. ImageJ Volume Viewer interpretations of the micro-computed tomography (μCT) data of two 6 mm diameter medallions from a stage C4 animal with epizootic shell disease (ESD). (A) Carapace medallion Ha4 with a 500 μm diameter lesion. (B) Portion of a chela medallion Ha6 with a conical shaped lesion developed through the cuticle. Insets show select orthogonal sections.

Conclusions

A major message of the study is that μCT can be tremendously informative in exploring the imperfections in structure and development of the lobster cuticle. In particular, high throughput μCT of carapace-cuticle-medallions of the American lobster is suggested as an approach of choice to study lobster ESD-susceptible cuticle. Chela-cuticle-medallions are a poor object from which to obtain high resolution structural data on the relatively thin calcite and exocuticle layers due to the massive endocuticle thickness and dominance of the endocuticle in the total chela cuticle structure. Indeed, the calcite and exocuticle layers of the chela are similar in thickness to those in the carapace. However, the massive endocuticle of the chela creates shadow-blurring of the information in the relatively thin epicuticle- and exocuticle-computed voxel densities. The shadow blurring of surface data would thus decrease the effectiveness of using chela medallions in searching for and detailed characterizing of early subclinical lesions. However, measuring chela mineralization may be a valuable indicator of stored $CaCO_3$ that is passed on to the next stage.

Thinness of the calcite layer viewed in the carapace may be a diagnostic feature of vulnerability to ESD. In our admittedly limited study, calcite layer thinness is seen to be correlated with ESD and could also be diagnostic in a predictive sense of individuals that do not yet display ESD at all or in other regions of their cuticle. To establish this prediction objective, one would need to apply this approach in a truly high-throughput manner in populations that predictably would develop high ESD incidence, but now in analysis are lobsters that are superficially ESD free.

Seeing and characterizing a subclinical ESD lesion itself may not be a realistically achievable and quantifiable objective to use in predicting population vulnerability to ESD. It would require scanning too large an area of carapace cuticle at high resolution. The protocols to analyze the data to see the smallest lesions would be too time consuming in our experience. This might change with faster, more powerful computers. Rather, characterizing the calcite layer thinness or density is an achievable diagnostic feature that may define lobster cuticle health and the ability to predict the vulnerable fraction of the lobster population that will develop shell disease.

Here, we showed that a healthy calcite layer has the approximate density of KH_2PO_4, used as a calibration standard. This implies that there is additional lower density material in what we describe compositionally (Kunkel 2106) as a calcite layer, lowering its density from 2.71 to 2.34 g cm^{-3} of KH_2PO_4. This approximate density

was seen in all the so-called healthy cuticles observed in the present study, including calcite layers adjacent to ESD lesions. This emphasizes the fact that the cuticle adjacent to ESD lesions seems to maintain a reasonably characteristic and healthy density despite being in an ESD animal and even close to the edge of an ESD lesion. This also puts more emphasis on the thinness of the calcite layer rather than its density. Clearly, these characterizations need to be tested more comprehensively by studying a variety of carapace medallions from more populations of characterized health. With larger sample sizes, including the density standard may be an important reference to add accuracy to density measurements. The density feature, evaluated in high-throughput samples using μCT, in itself may turn out to be one standard of cuticle wellness that can be used diagnostically to evaluate a population's future vulnerability to ESD. In addition, the K bipthalate density standard used (1.64 g cm^{-3}) was found to be very close to the endocuticle density making it an important reference for measuring endocuticle density variation.

Using Raman spectrometry, which did not detect chitin in the calcite layer of the carapace cuticle, the calcite layer was clearly shown to be a part of the lobster carapace epicuticle. That layer clearly develops its mineralization after ecdysis, including the postecdysial application of cement from the dermal glands. This is consistent with the concept of the arthropod cuticle being a living compartment of the organism that develops in many ways postecdysis (Wigglesworth 1948, Locke 1961). The living-cuticle concept opens additional questions about functions of macromolecules associated with lobster epicuticle/calcite layer formation (Kunkel 2013). Of particular interest would be characterizing the macromolecules, organic materials, and potential mineral components added as the cement layer to the epicuticle from the dermal glands, which are seen to be X-ray dense enough to be clustered as a cuticular component in canal contents (*see* fig. 6A in Kunkel et al. 2016; as well as the present study, Figs. 5D-a, 6A, B).

Irrespective of cuticle microbial flora (Feinman et al. 2017), it is likely that vulnerability of the cuticle to widely distributed flora will control whether ESD actually develops. If environmental stressors, such as ocean acidification, create a population of lobsters with increased vulnerability (e.g., due to thinness of the calcite layer), it is more likely that an opportunistic bacterium can nucleate the original subclinical lesion needed to allow ESD to develop.

The nature and causes of shell vulnerability need to be studied further. The newest model of the lobster carapace cuticle provided here (*see* Fig. 11) includes our latest insights into lobster shell that is the target of ESD. The features of this model were developed from observations on the cuticle made by many past investigators (reviewed by Kunkel 2013) with newer insights reported recently (Kunkel et al. 2016), as well as here. Many features of the model could contribute to vulnerability and development of shell disease. The immediate cause of shell disease may be the local thinness of the calcite layer, which allows a specific microbe, a combined consortium or dysbiosis of microbes (Meres et al. 2012) to attack, causing a subclinical lesion that is widened into a recognizable lesion by an even greater variety of microorganisms (Bell et al. 2012).

However, the underlying cause of ESD may derive from various sources. One cause could be the lack of sufficient $CaCO_3$ and carbonate apatite precursors that needed to be accumulated as cuticle components in the prior instar that would allow, on resorption and reuse, a healthy new cuticle to be established in a timely fashion and

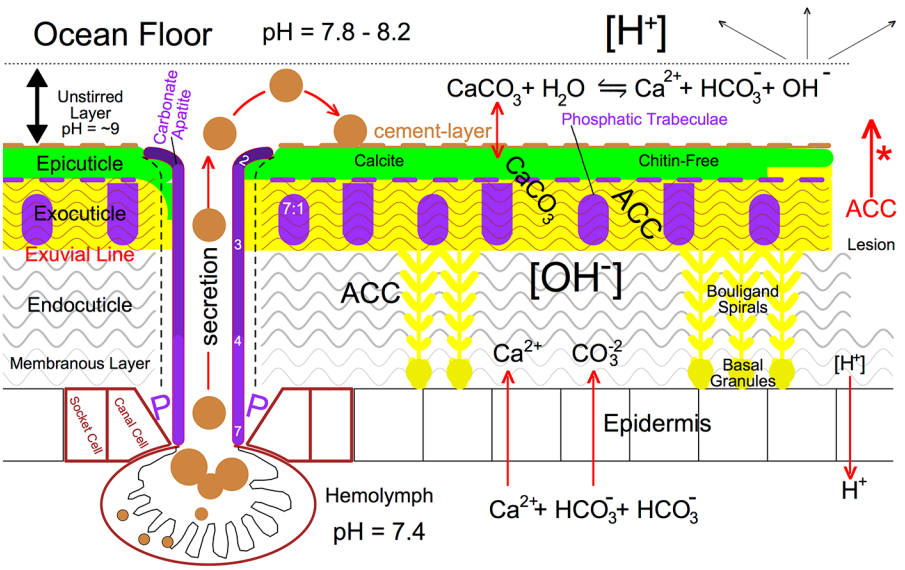

Figure 11. Interpretive model of American lobster, *Homarus americanus,* carapace cuticle and response to epizootic shell disease (ESD). This model version includes newly observed dynamic postmolt application of the cement layer by the dermal glands, recently described Bouligand swirls in the endocuticle and basal granules in a membranous layer (Kunkel et al. 2016). The cement layer moderates the dissolution of the shell's $CaCO_3$ allowing for an antimicrobial high pH unstirred layer. Aside from the Calcite ($CaCO_3$) layer of the Epicuticle and the stiff Phosphatic Trabeculae of the Exocuticle, the remaining bulk of the Bouligand layered cuticle is invested with relatively soft amorphous $CaCO_3$, (ACC) co-located with the chitin lamellae (wavy lines) as compact yellow (stalactites) in the exocuticle, seen as more diffuse yellow (Bouligand spirals) in the endocuticle and ending as basal granules in the membranous layer. Regional thinning of the calcite layer may lead to poor maintenance of the high-pH unstirred layer and greater vulnerability to ESD. A shell reacts to a lesion penetrating through the calcite layer by an increased flux (* red flux arrow) of (red/dissolving) ACC, more soluble than the crystalline-calcite form of $CaCO_3$. The more rapid dissolution of ACC increases the unstirred layer pH, an evolution engineered defense against lesion development. As the model fails, opportunistic bacteria and other microorganisms aggressively digest the cuticle, the animals hemocoel is compromised and it dies.

promoting an ESD resistant cuticle. Unlike other marine organisms, which are dependent on the immediate ocean environment's $CaCO_3$ availability (Zeebe 2012), the lobster creates its shell from internal stores of $CaCO_3$, which depend on how prior stages have fared in accumulation of this valuable marine resource, which is being made more expensive to obtain due to ocean acidification. The lobster is one organism that can survive in undersaturated seawater (Lebrato et al. 2016), but our thesis is that the undersaturation may cause a decreased history of $CaCO_3$ storage in the endocuticle, which is likely a major source of mineral that is resorbed in D1–D3 and stored for biomineralizing the next stage's cuticle. Insufficient $CaCO_3$ or $MgCO_3$ recovery between stages from exo- and endocuticle could lead to vulnerability at some point when the recovered minerals from the old cuticle are insufficient to produce a secure new exocuticle. We see the carbonate apatite trabeculae of the new exocuticle to be the major structurally-rigid architecture of the cuticle (Kunkel et al. 2012, Kunkel 2013, Kunkel and Jercinovic 2013). We also see the endocuticle as a storage depot to allow accumulation of chitin and minerals that are additional mineral and polymer resources needed to allow for the, in general, 10% linear growth and 20% area growth of new exocuticle that happens suddenly at ecdysis in each molting

cycle. This deposition and resorption of $CaCO_3$ is seen as an energetic process that crustaceans must undergo every molting cycle (Ziegler et al. 2004, 2017). But in each molting cycle, they must reinvest extra chitin and minerals rapidly after ecdysis in a new exocuticle from an adequate resorbed resource that includes extra $CaCO_3$ derived by resorption from the prior cuticle, including endocuticle and membranous layer $CaCO_3$ deposits. In addition, the lobster eats its own shed cuticle soon after ecdysis, which has residual $CaCO_3$ and $MgCO_3$ already in its proper carbonate oxidation state. This adds to a lobsters natural diet, which includes shellfish high in mineral carbonates. Previous use of μCT (Kunkel et al. 2016) has identified structures, such as the stalactites in the exocuticle, Bouligand spirals in the endocuticle, and basal granules in the membranous layer, which appear based on their density to be composed of $CaCO_3$ that exist during the C4 stage of intermolt and which would likely be sources of resorbed $CaCO_3$ as molting is initiated. EMP scans of these layers at stage C4 (Kunkel et al. 2012) also demonstrate a substantial molar ratio of $MgCO_3$ that is contained in the inner layers of cuticle available for polymer and mineral resorption and reuse. Interestingly, the C4 lobster providing Ha4, 5, and 6 medallions from the high ESD area was not seen to have the membranous layer $CaCO_3$ basal granules and Bouligand spiral extensions of exocuticle stalactites into the endocuticle that were seen in the ESD population lobsters from outer Georges Bank (Kunkel et a. 2016). If the environmental availability of those minerals does not allow the endocuticle and membranous layers to accumulate the extra stored minerals, then the needed resources to establish an invulnerable new exocuticle may be lacking in a vulnerable population of lobsters. This stored-mineral-aspect of vulnerability may build up over a series of molting cycles until it becomes critical and the cuticle's vulnerability is breached by perhaps the normal cuticle flora or by encouraging a dysbiosis (Meres et al. 2012).

Another avenue to shell vulnerability could be an improper application of the cement layer that was visualized here being applied onto the new cuticle from dermal glands. The composition of this postecdysial applied component of the epicuticle has been shown to be of sufficient density to be detected with the X-ray dose that images the main mineral cuticle. In fact, the density of the canal contents is similar to that of the lobster's endocuticle (Kunkel et al. 2016). The cement is also independent of the contribution that is traditionally considered to be applied to the epicuticle from the pore canals, which service the epicuticle from the inside (Locke 1961).

The observation that a seemingly healthy-thick calcite layer was seen in a new cuticle, medallion Ha7, sampled from a prior stage ESD lobster (Fig. 7B) argues that environmental erosion of the calcite after this early phase of the new cuticle may be important to ESD vulnerability. It could also be due to a clinically improper application of the postmolt protective cement layer. Measuring the postecdysial thinning of the calcite layer due to ocean acidification is one potential avenue of research that may provide insight into the development of vulnerability. Using a high-throughput procedure like μCT to follow carapace cuticle development and correlating it with local contemporaneous historical environmental data, such as temperature, calcium availability, and pH, may be the only way we can understand how and why ESD develops in one local population and not in another.

The ESD prediction approach depends on a high-throughput data sampling method, such as the particular model of μCT used here that provides a multi-position autosampler, but also depends on rapid high-throughput analysis. We examined

several analytic protocols, which were informative on individual specimens, but which were too time consuming to be dynamically applied to keep up with a high sampling rate. We compared the slow-methods to methods that are directed at rapidly establishing statistics, such as thinness or density of the calcite or other layers. Collection of μCT data from lobster carapace medallions sampled from lobsters of different developmental stages from different populations of variable ESD vulnerability would create a database as described in previous structural studies (Shields et al. 2012, Kunkel et al. 2016). Earlier contributions of cuticle structural detail to such a database resource was not feasible due to the preparation and analysis time, but μCT of plunge frozen cuticle medallions may provide the high enough throughput that enables structural data to be accumulated for such a database. It would allow tailor made rapid questions to be asked using fast ImageJ macros that could mine the data to test hypotheses on determinants of ESD, some of which have been presented here. We argue here for the enhancement of such a database with μCT data with appropriate metadata on age and environmental parameters that can help understand current lobster population vulnerabilities as they change.

Acknowledgments

The research associated with this project was supported by NOAA grant NA06NMF4720100 to RI SeaGrant supporting the New England Lobster Research Initiative. Vertebrate bone reference material was dissected and provided by P Pajevic.

Literature Cited

Bell SL, Allam B, McElroy A, Dove A, Taylor GT. 2012. Investigation of epizootic shell disease in American lobsters (*Homarus americanus*) from Long Island Sound: I. Characterization of associated microbial communities. J Shellfish Res. 31(2):473–484. https://doi.org/10.2983/035.031.0207

Castro KM, Factor JR, Angel T, Landers DF Jr. 2006. The conceptual approach to lobster shell disease revisited. J Crustac Biol. 26(4):646–660. https://doi.org/10.1651/S-2761a.1

Castro KM, Cobb JS, Gomez-Chiarri M, Tlusty MF. 2012. Epizootic shell disease in American lobsters *Homarus americanus* in southern New England: past, present and future. Dis Aquat Organ. 100(2):149–158. https://doi.org/10.3354/dao02507

Feinman SG, Martínez AU, Bowen JL, Tlusty MF. 2017. Fine-scale transition to lower bacterial diversity and altered community composition precedes shell disease in laboratory-reared juvenile American lobster. Dis Aquat Organ. 124(1):41–54. https://doi.org/10.3354/dao03111

Glenn RP, Pugh TL. 2006. Epizootic shell disease in American lobster (*Homarus americanus*) in Massachusetts coastal waters: interactions of temperature, maturity, and intermolt duration. J Crustac Biol. 26(4):639–645. https://doi.org/10.1651/S-2754.1

Golub GH, Reinsch C. 1970. Singular value decomposition and least squares solutions. Numerical Mathematics. 14:403–420. Golub GH, Reinsch C. 1970. Singular value decomposition and least squares solutions. Numerical Mathematics. 14:403–420.

Hostens J, Laperre K. 2015. High resolution microCT in preclinical applications. Accessed October 20, 2017. https://www.bruker.com/service/education-training/webinars/pci-webinars/high-resolution-microct-webinar.html

Kavukcuoglu NB, Patterson-Buckendahl P, Mann AB. 2008. Effect of osteocalcin deficiency on the nanomechanics and chemistry of mouse bones. J Mechanical Behavior Biomedical Materials. 2(4):348–354. https://doi.org/10.1016/j.jmbbm.2008.10.010

Kunkel JG. 2013. Modeling the calcium and phosphate mineralization of American lobster cuticle. Can J Fish Aquat Sci. 70(11):1601–1611. https://doi.org/10.1139/cjfas-2013-0034

Kunkel JG, Jercinovic MJ, Callaham DA, Smolowitz R, Tlusty MF. 2005. Electron microprobe measurement of mineralization of American lobster, *Homarus americanus*, cuticle: Proof of concept. 2005 Lobster Shell Disease Workshop, UMass Boston, MA. New England Aquarium. Aquatic Forum Series. p. 76–82. Accessed August 3, 2017. http://www.bio.umass.edu/biology/kunkel/pub/reprints/LobsterWorkshopMS-jgk.pdf

Kunkel JG, Nagel W, Jercinovic MJ. 2012. Mineral fine structure of the American lobster cuticle. J Shellfish Res. 31(2):515–526. https://doi.org/10.2983/035.031.0211

Kunkel JG, Jercinovic MJ. 2013. Carbonate apatite formulation in cuticle structure adds resistance to microbial attack for American lobster. Mar Biol Res. 9(1):27–34. https://doi.org/10.1080/17451000.2012.727427

Kunkel JG, Rosa M, Bahadur AN. 2015. Toward a modern interpretation of the American lobster shell using X-ray tomography. The Lobster Newsletter 28(2):19–21. Accessed August 3, 2017. http://www.fish.wa.gov.au/Documents/rock_lobster/the_lobster_newsletter/lobster_newsletter_v28_no2.pdf

Kunkel JG, Rosa M, Bahadur AN. 2016. 3D-Xray-tomography of American lobster shell structure: an overview. Fish Res. 186(1):372–382. http://dx.doi.org/10.1016/j.fishres.2016.09.028

Kunkel JG, Tlusty M, Jercinovic MJ. 2013. Fluoride role in carbonate apatite structures in exoskeletons of clawed lobsters, *Homarus americanus* and *Homarus gammarus*. Aquaculture 2013, Nashville TN. Accessed August 3, 2017. https://www.was.org/meetings/SessionAbstracts.aspx?Code=AQ2013&Session=37

Laufer H, Chen M, Johnson M, Demir N, Bobbitt JM. 2012. The effect of alkylphenols on lobster shell hardening. J Shellfish Res. 31(2):555–562. https://doi.org/10.2983/035.031.0215

Lebrato M, Andersson AJ, Ries JB, Aronson RB, Lamare MD, Koeve W, Oschlies A, Iglesias-Rodriguez MD, Thatje S, Amsler M, et al. 2016. Benthic marine calcifiers coexist with $CaCO_3$-undersaturated seawater worldwide. Global Biogeochem Cycles. 30(7):1038–1053. https://doi.org/10.1002/2015GB005260

Locke M. 1961. Pore canals and related structures in insect cuticle. J Biophys Biochem Cytol. 10(4):589–618. https://www.ncbi.nlm.nih.gov/pmc/articles/PMC2225106/. https://doi.org/10.1083/jcb.10.4.589

Maine DMR (Department of Marine Resources). 2017a. Maine lobster management zones. Available from: http://www.maine.gov/dmr/science-research/species/lobster/seasampling.html

Maine DMR (Department of Marine Resources). 2017b. 2017 monitoring program update. Available from: http://www.maine.gov/dmr/science-research/species/lobster/documents/2017monitoring.pdf

Mandel C. 2016. New England lobsters swim to Canada, bringing jobs with them. National Observer. June 1, 2016. Accessed October 22, 2017. Available from: https://www.nationalobserver.com/2016/06/01/news/new-england-lobsters-swim-canada-bringing-jobs-them

Meres NJ, Ajuzie CC, Sikaroodi M, Vemulapalli M, Shields JD, Gillevet PM. 2012. Dysbiosis in epizootic shell disease of the American lobster (*Homarus americanus*). J Shellfish Res. 31(2):463–472. https://doi.org/10.2983/035.031.0206

NOAA (National Oceanic and Atmospheric Administration). 2009 North Cape oil spill. Damage assessment, remediation and restoration program. Accessed August 20, 2017. Available from: https://darrp.noaa.gov/oil-spills/north-cape

Perry AL, Low PJ, Ellis JR, Reynolds JD. 2005. Climate change and distribution shifts in marine fishes. Science. 308(5730):1912–1915. https://doi.org/10.1126/science.1111322

Rao CR. 1965. Linear statistical inference and its applications. John Wiley & Sons, New York. 522 p.

Shields JD, Wheeler KN, Moss JA. 2012. Histological assessment of the lobster (*Homarus americanus*) in the "100 Lobsters" project. J Shellfish Res. 31(2):439–447. https://doi.org/10.2983/035.031.0204

Smolowitz R, Chistoserdov AY, Hsu A. 2005. A description of the pathology of epizootic shell disease in the American lobster, *Homarus americanus* H. Milne Edwards, 1837. J Shellfish Res. 24(3):749–756. https://doi.org/10.2983/0730-8000(2005)24[749:ADOTPO]2.0.CO;2

Steneck RS, Wahle RA. 2013. American lobster dynamics in a brave new ocean. Can J Fish Aquat Sci. 70(11):1612–1624. https://doi.org/10.1139/cjfas-2013-0094

Stevens BG. 2009. Effects of epizootic shell disease in American lobster *Homarus americanus* determined using a quantitative disease index. Dis Aquat Organ. 88(1):25–34. https://doi.org/10.3354/dao02135

Tlusty M, Smolowitz RM, Halvorson HO, DeVito SE. 2007. Host susceptibility hypothesis for shell disease in American lobsters. J Aquat Anim Health. 19(4):215–225. https://doi.org/10.1577/H06-014.1

University of Maine. 2017. Longer, stronger summers in the Gulf of Maine. ScienceDaily, 5 September 2017. Available from: http://www.sciencedaily.com/releases/2017/09/170905202951.htm

Waddy SL, Aiken DE, De Kleijn DPV. 1995. Control of growth and reproduction. Chapter 10. *In:* Factor JR, editor. Biology of the lobster. Elsevier. p. 217–266.

Wigglesworth VB. 1948. The insect cuticle as a living system. Discuss Faraday Soc. 3:172–177. https://doi.org/10.1039/df9480300172

Zeebe RE. 2012. History of seawater carbonate chemistry, atmospheric CO_2, and ocean acidification. Annu Rev Earth Planet Sci. 40:141–165. https://doi.org/10.1146/annurev-earth-042711-105521

Ziegler A, Weihrauch D, Hagedorn M, Towle DW, Bleher R. 2004. Expression and polarity reversal of V-type H^+-ATPase during the mineralization-demineralization cycle in *Porcellio scaber* sternal epithelial cells. J Exp Biol. 207:1749–1756. https://doi.org/10.1242/jeb.00953

Ziegler A, Neues F, Janacek J, Beckmann F, Epple M. 2017. Mineral in skeletal elements of the terrestrial crustacean *Porcellio scaber*: SRmCT of function related distribution and changes during the moult cycle. Arthropod Struct Dev. 46(1):63–76. https://doi.org/10.1016/j.asd.2016.05.004